

# What mesoscale signal does the altimeter reflect? On the decomposition in baroclinic modes and on a surface-trapped mode

GUILLAUME LAPEYRE

*Laboratoire de Météorologie Dynamique/IPSL, Ecole Normale Supérieure/CNRS, Paris, France*

## ABSTRACT

This study is motivated by the ongoing debate on the dynamical properties of surface motions at mesoscales that are measured by altimetry (for SSH) and microwave (for SST). The mesoscale signal seen by the altimeter is often considered to be associated with the first baroclinic mode, but recent results indicate that SST spectra and kinetic energy spectra derived from SSH have the same slope which is not consistent with this hypothesis. Moreover baroclinic modes are associated by definition with vanishing buoyancy anomalies at the ocean surface which is obviously not the case. Here a careful derivation of the vertical modes is done using the concepts of quasi-geostrophic potential vorticity (QG PV) theory. It is shown that the surface condition linking the streamfunction derivative and surface buoyancy necessitates to add a surface-trapped mode with no interior QG PV. The decomposition of a geostrophic flow on baroclinic modes alone is therefore incomplete and a complete decomposition involves both the surface mode and the barotropic/baroclinic modes. The surface mode is the generalization of a Surface QG (SQG) solution and is not orthogonal in the standard sense with baroclinic modes as it strongly projects at mesoscales on the first baroclinic mode. These results are illustrated with analytical examples and with a realistic simulation of the North Atlantic ocean. The surface mode is shown to be as energetic as the interior modes in the OGCM simulation. Moreover it dominates the surface mesoscale signal in most of the active regions of the Atlantic. On the other hand, the first baroclinic mode becomes dominant at depth as expected by previous results of the literature. The dominance of the surface mode at the surface is shown to be determined at first order by the large-scale forcing of PV and surface buoyancy. These results point out the necessity of a new interpretation of the surface dynamics and its coupling with the ocean interior for turbulent flows at mesoscales.

## 1. Introduction

The global coverage of satellite measurements of Sea Surface Height and Sea Surface Temperature (and in some years Sea Surface Salinity) highlights the need to better clarify the link between the surface signal and the interior dynamics. This would allow a better assimilation of the surface signal in operational models as the surface signal could be propagated into the interior. Indeed some attempts have been done in that direction using vertical EOFs (e.g. De Mey and Robinson 1987) but we still need dynamical constraints to improve the method. It is generally thought that mesoscale motions at the ocean surface are strongly related to the first baroclinic mode. This conjecture was proposed by Stammer (1997) as he observed that the lengthscale of zero-crossing of the spatial autocorrelation of the SSH was proportional to the first Rossby deformation radius. This “suggests that first-mode processes dominate observed SSH fluctuations” (Stammer 1997). In addition, Wunsch (1997) examined the partition of kinetic energy obtained by current meters into vertical modes and showed that “surface kinetic energies are

dominated by the first baroclinic mode”. These results from direct observations were also confirmed in some manner by numerical simulations. Smith and Vallis (2001) show, in simulations of multi-layer quasi-geostrophic turbulence, that the first baroclinic mode dominates the barotropic mode for mesoscale kinetic energy for a stratification with a thermocline. This was not the case for a stratification with constant Brunt-Väisälä frequency. A somewhat similar result was obtained by Scott and Arbic (2007) for a two-layer model of quasi-geostrophic turbulence. Recently, Scott and Wang (2005) have computed the spectral kinetic eddy flux from altimetry and showed that it was associated with an inverse energy cascade at ocean surface. This was also confirmed by Schlosser and Eden (2007) in a numerical simulation of the North Atlantic. The standard theory of geostrophic turbulence states that the baroclinic mode should have a direct cascade, so there is some paradox between this result and the general assumption relating the surface motions with the baroclinic mode. Scott and Arbic (2007) proposed an explanation based on the fact that there can be upscale fluxes of baroclinic kinetic energy when a thermocline is present.

However an alternative scenario can be proposed from the results of Lapeyre and Klein (2006a). This study shows that the vertical mode decomposition is incomplete as one

---

*Corresponding author address:*

G. Lapeyre, LMD/IPSL, Ecole Normale Supérieure, 24 Rue Lhomond, 75005 Paris, France (glapeyre@lmd.ens.fr)

should take into account the boundary condition at the ocean surface. This condition states that surface density is proportional to the vertical derivative of the streamfunction and induces a surface-trapped mode, known as a Surface Quasi-Geostrophic mode, for which interior QG PV is uniform. Lapeyre and Klein (2006a) show that, in a numerical simulation of an unstable baroclinic front, the SQG solution tends to dominate in the first 500 meters of the ocean. Additional evidence of the pertinence of the SQG model for the upper ocean mesoscales was shown by reconstruction of velocity field from SST field using satellite or *in situ* observations (Isern-Fontanet et al. 2006; LaCasce and Mahadevan 2006) or using numerical simulations (Lapeyre and Klein 2006a; LaCasce and Mahadevan 2006; Klein et al. 2007; Isern-Fontanet et al. 2007). Another evidence of the pertinence of the SQG solution is its associated upscale flux of surface kinetic energy (Capet et al. 2007; Klein et al. 2007), which may explain Scott and Wang (2005) finding. A source of kinetic energy at meso and submesoscales (due to frontogenesis processes) compensates this flux so that the surface kinetic energy cascades downscale (Capet et al. 2007). It is therefore plausible that the surface motions may represent SQG motions. However this theory does not take into account the interior PV anomalies that may also be important for the dynamics. Another important aspect of the study of Lapeyre and Klein (2006a) is that the kinetic energy and SST spectra should have the same slope at mesoscale, which was confirmed by comparison of altimetry and microwave SST (Isern-Fontanet et al. 2006) and in an OGCM simulation (Isern-Fontanet et al. 2007). This behavior cannot be explained if the surface were associated with the first baroclinic mode. In that case, the SST (or the potential energy in the upper layers) spectrum should be steeper than KE as observed in idealized simulations which have no surface buoyancy anomaly (Smith and Vallis 2001). This tends to favor the interpretation of Lapeyre and Klein (2006a) about the importance of the surface mode for mesoscale dynamics.

To better understand what represents the surface motions, a decomposition of the mesoscale dynamics of a simulation of the North Atlantic Ocean into vertical modes is performed taking into account the proper surface condition. The model used here is the POP model at  $1/10^\circ$  (Smith et al. 2000; Bryan et al. 2007) that resolves the mesoscale dynamics with realistic forcing and is suitable for this type of study. A comparison with TOPEX altimeter data has indeed shown that it had similar characteristics in terms of energy and lengthscales (Brachet et al. 2004). In Section 2, the vertical modes are carefully derived with the introduction of the surface-trapped mode that satisfy the surface boundary condition. The argument is similar to the one of Dutton (1974), Held et al. (1985) and Tung and Welch (2001): when one uses modal decomposition for a Sturm-Liouville problem, the boundary conditions are crucial for the existence and completeness of the eigenvectors of the problem. If not, a continuous spectrum of eigenvalues is necessary to close the problem. If the modes verify homogeneous boundary conditions and if the solution we seek satisfies inhomogeneous boundary conditions, the convergence of the expansion in modes is not uniform (Held et al. 1985). It will be shown

that the interior modes are completed with a surface-trapped solution. Both types of modes (interior and surface) have a signature at the surface in terms of velocity field, but only the surface trapped solution has a signature in density at the surface. In Section 3, some aspects of a complete decomposition involving the surface mode will be detailed. This technique will be applied in Section 4 to examine the output of a realistic simulation of the North Atlantic Ocean to see whether the surface trapped mode dominates the total solution at the ocean surface. Results will be discussed and interpreted in Section 6. Finally conclusions will be drawn.

## 2. Posing the problem

In physical oceanography, the splitting between horizontal and vertical coordinates is often used with the help of vertical modes. Its application for the QG theory was first done by Charney (1971), then discussed by Dutton (1974), Flierl (1978) and Philander (1978) among others. The vertical modes appear as a byproduct of the QG potential vorticity (as shown below). The QGPV is

$$PV = f + \nabla^2 \psi + \frac{\partial}{\partial z} \left( \frac{f_0^2}{N^2} \frac{\partial \psi}{\partial z} \right) \quad (1)$$

where  $\psi$  is the streamfunction,  $f$  the Coriolis parameter ( $f_0$  its value at a given latitude) and  $N$  the Brunt-Väisälä frequency. QGPV is conserved along geostrophic Lagrangian trajectories in absence of forcing and dissipation:

$$\frac{\partial PV}{\partial t} + \mathbf{u} \cdot \nabla PV = 0 \quad (2)$$

with  $\mathbf{u} = (-\partial\psi/\partial y, \partial\psi/\partial x)$ . The linear operator in (1) that passes from streamfunction to PV is elliptic in general (because  $N^2 > 0$  in stable stratification). To obtain the streamfunction, (1) needs to be inverted under proper boundary conditions, and in particular at the ocean surface. These conditions are associated with prognostic equations to complete the QG model and can be obtained using the hydrostatic and QG balances

$$b = f_0 \frac{\partial \psi}{\partial z} \quad (3)$$

where  $b = -g\rho/\rho_0$  is buoyancy anomaly and  $\rho$  is density. Linearizing surface pressure equation

$$p_{atm} = p(x, y, z = 0) - \rho_0 g h \quad (4)$$

where  $h$  is Sea Surface Height (SSH), the equation of SSH and surface buoyancy are

$$\left( \frac{\partial}{\partial t} + \mathbf{u}_s \cdot \nabla \right) h = w \quad (5a)$$

$$\left( \frac{\partial}{\partial t} + \mathbf{u}_s \cdot \nabla \right) b_s = -N_s^2 w \quad (5b)$$

where  $\mathbf{u}_s$  is the horizontal velocity,  $b_s$  buoyancy,  $w$  is the vertical velocity, all evaluated at the ocean surface ( $z = 0$ ). The evolution of the surface fields are then

$$\left( \frac{\partial}{\partial t} + \mathbf{u}_s \cdot \nabla \right) \left( \frac{\partial \psi}{\partial z} + \frac{N_s^2}{g} \psi \right) = 0. \quad (6)$$

In the rigid lid case, this condition simplifies into

$$\left(\frac{\partial}{\partial t} + \mathbf{u}_s \cdot \nabla\right) \frac{\partial \psi}{\partial z} = 0. \quad (7)$$

at  $z = 0$ . The surface boundary condition is thus given by

$$b_s = f_0 \left. \frac{\partial \psi}{\partial z} \right|_{z=0} \quad (8)$$

With this condition<sup>1</sup>, it is possible to invert PV and have a fully prognostic QG model.

To invert (1) and (8), it is useful to split the solution in two parts  $\psi_{int}$  and  $\psi_{sur}$  (see Lapeyre and Klein 2006a, for more details),

$$f + \nabla^2 \psi_{int} + \frac{\partial}{\partial z} \left( \frac{f_0^2}{N^2} \frac{\partial \psi_{int}}{\partial z} \right) = PV \quad (9)$$

$$\left. \frac{\partial \psi_{int}}{\partial z} \right|_{z=0} = 0$$

and

$$\nabla^2 \psi_{sur} + \frac{\partial}{\partial z} \left( \frac{f_0^2}{N^2} \frac{\partial \psi_{sur}}{\partial z} \right) = 0 \quad (10)$$

$$\left. \frac{\partial \psi_{sur}}{\partial z} \right|_{z=0} = \frac{b_s}{f_0}$$

These two solutions are related to two different problems:  $\psi_{int}$  is associated with interior PV anomalies with no surface buoyancy anomalies. This is the standard paradigm of PV layers in the Phillips model of baroclinic instability.  $\psi_{sur}$  is associated with the surface buoyancy anomaly with uniform interior PV. This is the standard paradigm of surface anomalies in the Eady problem of baroclinic instability. The surface buoyancy plays the same role as an interior PV if it is replaced with a Dirac distribution (Bretherton 1966).

The classical vertical modes (barotropic and baroclinic) actually appear when one solves (9) by separating the horizontal and vertical components. These modes, that will be noted  $F_j(z)$ , verify a Sturm-Liouville equation with eigenvalues  $-\lambda_j^{-2}$ ,

$$\frac{\partial}{\partial z} \left( \frac{f_0^2}{N^2} \frac{\partial F_j}{\partial z} \right) = -\lambda_j^{-2} F_j \quad (11a)$$

$$\left. \frac{\partial F_j}{\partial z} \right|_{z=0} = 0 \quad (11b)$$

where  $\lambda_j$  are the Rossby deformation radii. The deformation radii were computed (at least for the first baroclinic one) for different regions of the world ocean (Chelton et al. 1998, and references therein). Using the vertical modes  $F_j$ , the solution of (9) can be written as

$$\psi_{int}(x, y, z) = \sum_j \phi_j(x, y) F_j(z) \quad (12)$$

<sup>1</sup>There is also a similar condition at the bottom of the ocean but only the case of vanishing buoyancy anomaly at depth will be considered. The horizontal boundary conditions correspond to a doubly-periodic ocean. This should not modify the argument.

with

$$\nabla^2 \phi_j - \lambda_j^{-2} \phi_j = \int_{-H}^0 PV(x, y, z) F_j(z) dz \quad (13)$$

The modal decomposition is also done for the theory of linear inertia-gravity waves for which the boundary conditions are different (see Gill 1984). Here, the modes  $F_j$  allow to solve equations (1) and (8) associated with prognostic equations (2) and (7), in the case of linear Rossby waves. In this situation and for the linear baroclinic instability problem for a resting ocean with flat bottom (see e.g. Flierl 1978), the buoyancy equation at the surface (7) reduces to

$$\frac{\partial}{\partial t} \frac{\partial \psi}{\partial z} = 0 \quad (14)$$

and  $\partial_z \psi$  vanishes at the ocean surface. Therefore, linear Rossby waves do not need a solution for  $\psi_{sur}$ . Other modes, but with special properties at the ocean surface, can be obtained in the case of surface intensified motions (McWilliams and Shen 1980). For nonlinear dynamics, such as driven by mesoscale eddies, the surface equation is fully nonlinear and one cannot a priori neglect surface buoyancy anomalies. In fact, SST (and surface mesoscale buoyancy anomalies drive a rich submesoscale dynamics associated with high relative enstrophy and strong frontogenesis (Lapeyre et al. 2006; Lapeyre and Klein 2006b; Klein et al. 2007).

The dynamics associated with  $\psi_{sur}$  has been extensively studied in the atmospheric context of the Eady model (uniform PV between two horizontal surfaces and constant  $N^2$ ). It can be called a surface trapped mode because it corresponds to a solution decreasing with depth. In the case of constant  $N^2$ , the solution is just

$$\widehat{\psi}_{sur}(\mathbf{k}, z) = \frac{\widehat{b}_s(\mathbf{k})}{kN} \exp\left(\frac{Nkz}{f_0}\right) \quad (15)$$

for an infinite ocean. Here  $\widehat{(\ )}$  denotes horizontal Fourier transform,  $\mathbf{k}$  is the horizontal wavevector and  $k$  is its modulus. This is a SQG solution which decays exponentially with depth. The smaller horizontal structures (large  $k$ ) have a smaller decay scale, which preserves the 3-D isotropy. A property of this system is that buoyancy and kinetic energy have the same spectra at the ocean surface. Also, the vertical structure is scale-dependent contrary to baroclinic modes for which the vertical structure is independent on the horizontal scale. This is due to the constraint of uniform PV. More details on this type of solution can be found in Held et al. (1995) and Lapeyre and Klein (2006a).

In the oceanic context, standard QG turbulence simulations do not have considered motions associated with  $\psi_{sur}$  because they all assume no buoyancy anomaly at the surface (McWilliams and Chow 1981; Hua and Haidvogel 1986; Smith and Vallis 2001). The same shortcoming exists for analysis of observations (McWilliams et al. 1986; Wunsch 1997, among others). Only recent studies of stratified turbulence (Lapeyre and Klein 2006a; Lapeyre et al. 2006; Klein et al. 2007) have highlighted the important role of surface

buoyancy anomalies for the dynamics of upper oceanic layers.

Therefore the geostrophic flow  $\psi$  cannot be a priori decomposed into vertical modes  $F_j$ , because these modes forbid the existence of a surface buoyancy anomaly. In this sense, they are “incomplete”. Decomposing  $\psi(x, y, z)$  into vertical modes neglecting the boundary condition is equivalent to project the surface mode  $\psi_{sur}$  on the vertical barotropic/baroclinic modes: the reconstructed field will not verify the surface condition (8) for buoyancy, even if the reconstructed streamfunction may resemble the true streamfunction. As a result, part of the total energy may not be captured.

### 3. Complete and incomplete decomposition

Using the results of the preceding section, a “complete” decomposition of a geostrophic flow must be written as

$$\widehat{\psi}(\mathbf{k}, z) = \widehat{\gamma}(\mathbf{k})\widehat{E}(k, z) + \sum_{j=0}^n \widehat{\alpha}_j(\mathbf{k})F_j(z) \quad (16)$$

The first term on the right hand side corresponds to the “surface mode” whereas the sum corresponds to the “interior modes” (barotropic and baroclinic). For each wavenumber  $k$ ,  $\widehat{E}(k, z)$  verifies

$$-k^2\widehat{E} + \frac{\partial}{\partial z} \left( \frac{f_0^2}{N^2} \frac{\partial \widehat{E}}{\partial z} \right) = 0 \quad (17)$$

with  $\partial_z \widehat{E} = 1$  at  $z = 0$  and  $\partial_z \widehat{E} = 0$  at  $z = -H$ . The decomposition (16) will be called “complete” since it takes into account the surface condition. Details concerning the technical aspect decomposition are given in the Appendix and it was validated on two test cases: one with a surface mode and a baroclinic mode with a constant  $N^2$ , the other one with an exponential stratification profile with only a baroclinic mode (not shown). An “incomplete” decomposition consists in finding the coefficients  $\widehat{\beta}_j(\mathbf{k})$  that satisfy

$$\widehat{\psi}(\mathbf{k}, z) = \sum_{j=0}^n \widehat{\beta}_j(\mathbf{k})F_j(z) \quad (18)$$

The solution of such a problem will not verify the surface condition since  $\partial_z F_j = 0$  at the surface. The coefficients  $\widehat{\beta}_j(\mathbf{k})$  can be found by the relation

$$\widehat{\beta}_j(\mathbf{k}) = \int_{-H}^0 F_j(z) \widehat{\psi}(\mathbf{k}, z) dz \quad (19)$$

Figure 1b represents the first three vertical modes and the surface modes for three different wavelength for the Gulf Stream stratification that will be examined more in details in Section 4a. Its stratification is shown in Fig. 1a. The vertical profiles of the modes are typical and do not change qualitatively in other regions. The first baroclinic mode corresponds to a Rossby deformation radius of 31 km and has its zero-crossing at 900 m. The second baroclinic mode has a deformation radius of 13 km with two zero crossings, one

at 300 m and another one at 1540 m. The first 7 baroclinic modes are intensified in the first two thousands of meters (not shown) due to the presence of the thermocline. The surface mode  $\widehat{E}(k, z)$  is also intensified in the first 1000 meters for wavelengths between 30 and 550 km and decays with depth. The smaller wavelengths are associated with the stronger decay as consistent with SQG solution (15). Also the presence of a strong barotropic component for larger wavelengths can be noted.

To see whether the surface mode can be mistaken with interior baroclinic modes, the projection of  $\widehat{E}$  onto the modes  $F_n$  can be computed. This gives an “incomplete” decomposition

$$\widehat{E}(k, z) = \sum_{j=0}^n \widehat{\beta}_j(k)F_j(z) + residue \quad (20)$$

Dividing by  $\widehat{E}(k, z=0)$  and evaluating at  $z = 0$  gives

$$1 = \sum_{j=0}^n \frac{\widehat{\beta}_j(k)F_j(0)}{\widehat{E}(k, 0)} + \frac{residue}{\widehat{E}(k, 0)} \quad (21)$$

Figure 2a presents  $\widehat{\beta}_j(k)F_j(0)/\widehat{E}(k, 0)$  as a function of wavelength for the Gulf Stream stratification and using  $n = 7$ . The surface mode essentially projects on the first baroclinic mode for wavelengths smaller than 300 km. For lengthscales between 70 km and 300 km, this mode represents more than 45% of the signal. At larger scales, the surface mode essentially projects on the barotropic mode and this projection increases as wavelength increases. For lengthscales smaller than 180 km, the second contribution comes from the second baroclinic mode, while it comes from the barotropic mode for wavelengths between 180 km and 300 km. Using only 8 modes, the sum of the projections represents more than 95% of the signal for lengthscales larger than 90 km. For smaller lengthscales, there is some equipartition of the projection between all the baroclinic modes and the projection becomes incomplete. At 10 km, the residue represents more than 50% of the total which indicates that the interior modes are not able to quantitatively represent the surface mode at these scales. This demonstrates clearly that an incomplete decomposition will strengthen the baroclinic signal at mesoscales because the surface mode will be falsely added to the first baroclinic mode signal.

The case of a constant stratification  $N^2$  gives further insight on the degree of projection of the surface mode onto the interior modes. In that case, the surface mode writes

$$\widehat{E}(k, z) = \frac{H \cosh(x(z'+1))}{x \sinh(x)} \quad (22)$$

where  $x = NkH/f_0$  and  $z' = z/H$ . Its vertical derivative is

$$\frac{\partial \widehat{E}}{\partial z} = \frac{\sinh(x(z'+1))}{\sinh(x)} \quad (23)$$

which satisfies  $\frac{\partial \widehat{E}}{\partial z}(z=0) = 1$  and  $\frac{\partial \widehat{E}}{\partial z}(z=-H) = 0$ . The interior modes are

$$F_m(z) = \sqrt{\frac{2}{H}} \cos(m\pi z') \quad (24)$$

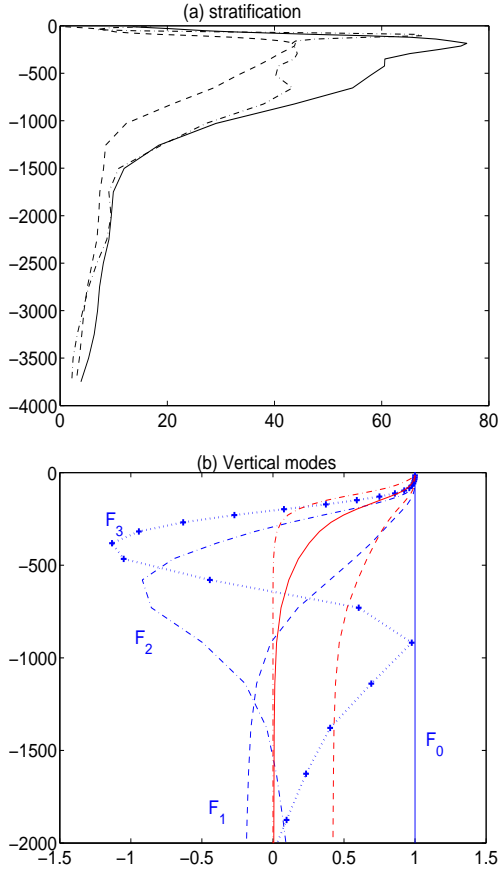


FIG. 1. (a) Vertical profile of  $N/f_0$  for three oceanic regions: continuous line: Gulf Stream; dashed line: North Atlantic Drift; dash-dotted line: Azores current. (b) First 4 interior modes  $F_j(z)$  (in blue) and surface mode  $\hat{E}(k = 2\pi/l, z)$  for  $l = 100$  km (red solid line),  $l = 550$  km (red dashed line),  $l = 30$  km (red dash-dotted line). The different curves have been normalized so that  $\psi = 1$  at  $z = 0$ . The modes were computed for the GS region.

for  $m \geq 1$  and  $F_0 = 1/\sqrt{H}$ . The projection of the surface mode on the interior modes gives

$$\hat{\beta}_0 = \int_{-H}^0 \hat{E} F_0 dz = \frac{H\sqrt{H}}{x^2} \quad (25)$$

and

$$\hat{\beta}_j = \int_{-H}^0 \hat{E} F_j dz = \frac{H\sqrt{2H}}{x^2 + j^2\pi^2} \quad (26)$$

for  $j \geq 1$ .

Figure 2b shows the ratio  $\hat{\beta}_j(k)F_j(z=0)/\hat{E}(k, z=0)$  using parameters  $N/f_0 = 50$  and  $H = 4000$  m. This model with constant stratification qualitatively reproduces the features obtained for realistic stratification (compare Fig. 2a and b). For  $x$  tending to zero, the ratio of  $\hat{\beta}_j(k)F_j(z=0)/\hat{\beta}_0(k)F_0(z=0)$  tends to zero for  $j \geq 1$ , which means that the barotropic mode entirely dominates the signal at large scales. This is because the vertical decay scale of  $\hat{E}$  is proportional to the horizontal scale so that the vertical decay is very weak for large scales. For  $x$  tending to infinity,  $\hat{\beta}_i(k)F_i(z=0)/\hat{\beta}_j(k)F_j(z=0)$  tends to 1 for  $i$  and  $j \geq 1$ , which means that there is equipartition of the projec-

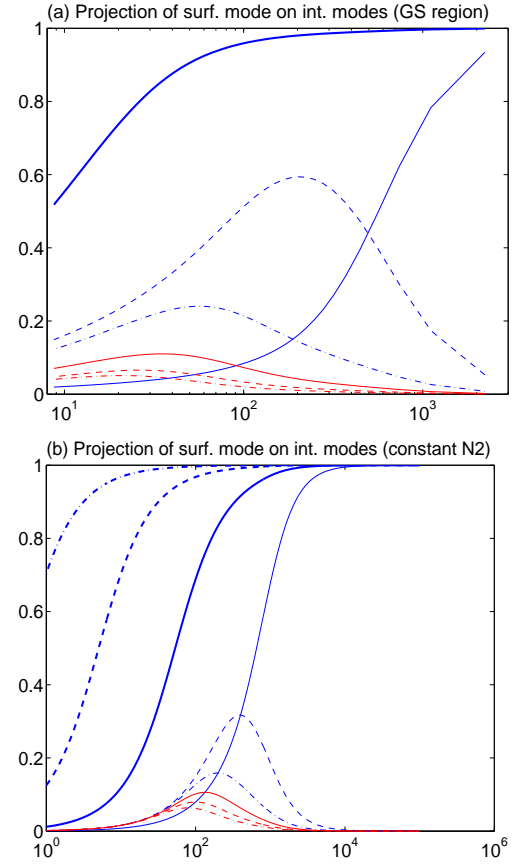


FIG. 2. Projection of the surface mode evaluated at  $z = 0$  into the interior modes as a function of wavelength (in km). (a) For GS region. (b) For analytical solution with constant  $N^2$ . Blue thin and solid line, barotropic mode  $j = 0$ ; blue dashed line, first baroclinic (BC) mode  $j = 1$ ; blue dotted line,  $j = 2$ . Red solid,  $j = 3$ ; red dashed,  $j = 4$ ; red dash-dotted,  $j = 5$ . The thick blue line is the sum of the first 8 interior modes. For figure (b) The thick dashed line is the reconstruction with 80 modes and the thick dash-dotted line is with 800 modes.

tions between the baroclinic modes for small scales. Moreover the barotropic contribution is twice smaller than the first baroclinic mode ( $\hat{\beta}_1(k)F_1(z=0)/\hat{\beta}_0(k)F_0(z=0) \rightarrow 2$ ), which explains why there is a range at mesoscale where the projection on the first baroclinic mode dominates. The baroclinic components are larger for a real stratification than for the constant  $N^2$  case. This may be due to the presence of a thermocline that is known to increase baroclinic motions intensified near the surface (Hua and Haidvogel 1986; Smith and Vallis 2001). Finally, as shown on Fig. 2b, increasing the number of interior modes allows to reconstruct the surface streamfunction down to a lengthscale that decays with the number of modes.

The reconstruction for different depths also provides some information on the degree of projection of the surface mode on the interior modes. Figure 3a shows the incomplete reconstruction of the surface mode streamfunction using 10, 100 and 1000 modes for a typical wavelength of 173 km (similar results are found for other wavelengths). Ten modes are not sufficient to correctly simulate the exponential decay of the streamfunction in the vertical. The quality of the re-

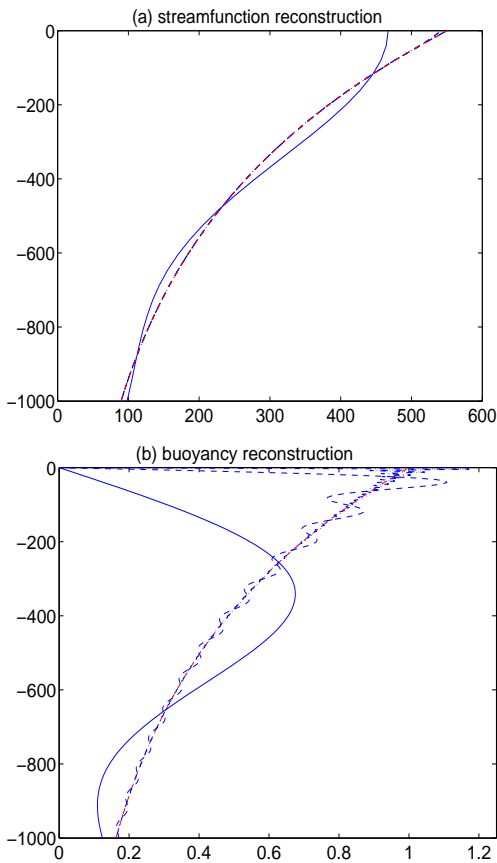


FIG. 3. (a) red solid line: vertical profile of the streamfunction  $\widehat{E}(k, z)$  for  $2\pi/k = 173$  km. Blue solid line: reconstruction using 10 interior modes  $F_j$ ; thin dashed line: using 100 modes; thin dash-dotted line: using 1000 modes. Reconstruction with 100 and 1000 modes superpose almost exactly with  $\widehat{E}(k, z)$ . (b) Same definition as in (a) but for  $\partial_z \widehat{E}(k, z)$ .

construction greatly improves for all depths when one passes to 100 or 1000 modes. The reconstruction of the vertical derivative of the streamfunction that serves to reconstruct the buoyancy (Fig. 3b) shows that the modes do not represent the surface condition (because they satisfy  $\partial_z F_j = 0$ ). The relative error for  $z < 0$  is quite large for all depths for a 10 mode reconstruction (larger than 50%) and the reconstruction is slow to converge, even with 100 modes (error of 8%). This is because the incomplete reconstruction is responsible of a Gibbs phenomenon at the ocean surface that creates oscillations in the reconstruction in the first hundreds of meters.

#### 4. Results

To quantify the importance of the surface mode, the output of a realistic simulation of the North Atlantic Ocean can be examined. The simulation used here was done with the POP model with a resolution of  $1/10^\circ$  of degree over a stretched vertical grid of 40 levels and is forced with realistic winds and heat fluxes. A daily average taken in January 2002 is made to filter a large part of near-inertial waves so that only the balance part of the flow can be examined.

The decomposition has been made on domains of  $10^\circ$  by  $10^\circ$  over the North Atlantic Ocean between  $30^\circ$  N and  $50^\circ$  N and  $70^\circ$  W and  $10^\circ$  W. The properties are qualitatively similar through the Atlantic Ocean and three sub-regions where the mesoscale activity is important are analyzed in details, one in the Gulf Stream (noted GS), one in the North Atlantic Drift (NAD) and a last one in the Azores Current (AC).

In each domain, data are interpolated on a grid of  $256 \times 256$  points, and then the box is made periodic using mirror symmetry for buoyancy in  $x$  and  $y$  (and reversing the sign of the velocity field to adequately preserve the thermal wind balance). To create missing data on islands and seamounts, the following procedure was applied: at each level, points where the bathymetry outcrops the level are replaced by a weighted mean over a region of  $2^\circ$  of longitude by  $2^\circ$  of latitude. The weight decays exponentially with the square of the distance. The velocity field obtained by this method is continuous on the horizontal which allows to use horizontal Fourier transforms (other details are provided in the Appendix). The results are not very sensitive to the details of the method as long as the bottom buoyancy anomalies are weak. The different decompositions were done using  $n = 7$  which gives sufficient good reconstruction as will be shown later.

First, the Brunt-Väisälä frequency is shown in Fig. 1a for these three regions. In the Gulf-Stream and the Azores current, a seasonal thermocline is present around 200-300 meters. The main thermocline is located at deeper levels ranging from 400 m for the North Atlantic Drift to 800 m for the Azores current. For each regions, the surface layers are weakly stratified because of the winter conditions.

##### a. Region near the Gulf Stream

The first region is located between  $70^\circ$  W and  $60^\circ$  W and between  $30^\circ$  N and  $40^\circ$  N in the Gulf Stream area. This region has a strong mesoscale activity with many eddy interactions. The kinetic energy is intensified at the surface and decays with depth (Fig. 5a). The buoyancy r.m.s. at mesoscale (for which wavelengths larger than 400 km have been filtered) has a maximum just underneath the mixed layer (at 200m) and decays with depth (Fig. 4a). These results confirm that the mesoscale activity is concentrated in the upper ocean and this may be attributed to the presence of a strong thermocline (Hua and Haidvogel 1986; Smith and Vallis 2001).

The complete and incomplete decompositions can be analyzed in terms of representing the total flow. Both methods are able to correctly represent the mean kinetic energy (KE) except in the first 80 meters (not shown). Concerning the buoyancy r.m.s., the reconstruction using the complete method is relatively good below the mixed layer and at the surface (Fig. 4a). However, it does not give the right variance at the bottom of the mixed layer. The situation is worse for the incomplete method. In that case, the buoyancy anomaly reconstruction vanishes at the surface and is quite small in the first 100 meters, so that there is a systematic error due to the reconstruction down to 400 meters. This error can still be detected down to 1100 m (on the contrary of the com-

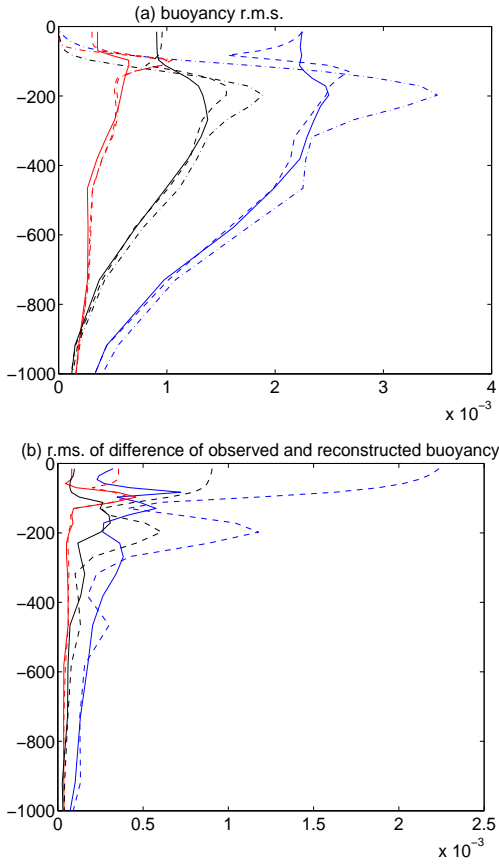


FIG. 4. (a) Vertical profile of the buoyancy r.m.s. (scales larger than 400 km have been filtered). Dashed line, reconstruction using complete method. Dash-dotted line, reconstruction using incomplete method. In blue, for GS, in red for AC and in black for NAD. (b) Vertical profile of the r.m.s. of the difference of reconstruction (solid line is complete and dashed line is incomplete method) for the three oceanic regions.

plete method which gives the right buoyancy r.m.s. below 500 m). The r.m.s. of the difference of the true buoyancy with its reconstruction confirms this result (Fig. 4b) since the complete reconstruction gives much smaller r.m.s for the first 300 meters than the incomplete reconstruction. This is consistent with the analytical decomposition example with constant  $N^2$  of Section 3 since the incomplete method is still able to reconstruct the kinetic energy but has more difficulty in reconstructing the buoyancy variance.

The kinetic energy of the different vertical modes (interior and surface) can be separately evaluated at different depths to determine their relative importance. A caveat is that the modes are not orthogonal in the sense that the scalar product of surface velocity of two different baroclinic modes  $\langle \mathbf{u}_i \cdot \mathbf{u}_j \rangle = \langle \nabla \alpha_i \cdot \nabla \alpha_j \rangle F_i(z=0) F_j(z=0)$  is not equal to zero because  $F_i(z=0) F_j(z=0) \neq 0$  for  $i \neq j$  (here  $\langle \rangle$  is the horizontal mean). This means that the sum of the surface kinetic energy of each mode is not the surface kinetic energy of the sum of the modes. As can be seen in Fig. 5a, in this region the kinetic energy of the surface mode dominates in the first 600 meters and is twice as large as the observed kinetic energy. The first baroclinic mode represents

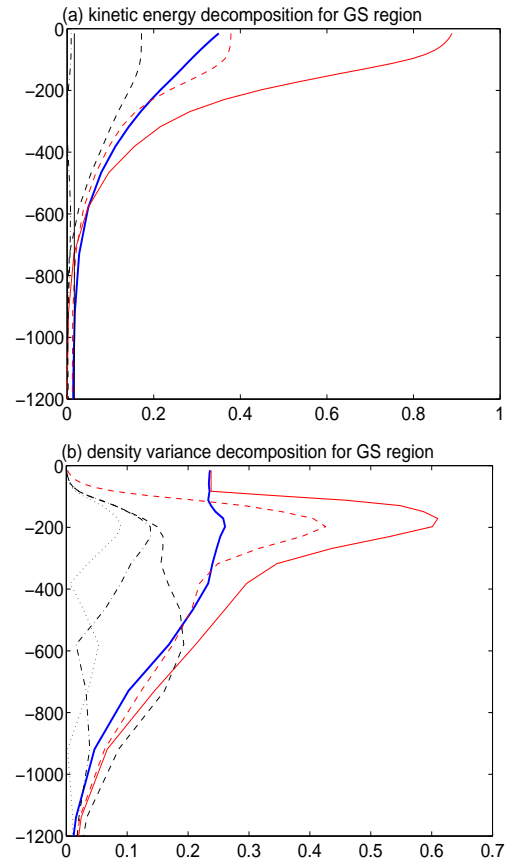


FIG. 5. (a) Vertical profile of the mean kinetic energy (in blue). Solid red line, KE of surface mode; red dash line, KE of the sum of interior modes; black continuous line, barotropic mode; dashed black line, first baroclinic mode; black dash-dotted line, second baroclinic mode. (b) Same meaning but for density variance. Dotted line represents the third baroclinic mode.

the second larger contribution, as large as the observed KE. In fact, as shown in Tab. 1, the first baroclinic and the surface modes are in opposing phase so that their contribution cancel each other. This explains why their energy is larger than the observed KE. The decomposition of the buoyancy variance (Fig. 5b) shows that the surface mode dominates the

Correlation	SMOD	IMOD	BT	BC1
vorticity GS	0.80	-0.50	-0.36	-0.42
NAD	0.77	-0.32	-0.13	-0.18
AC	0.57	0.81	0.30	0.66
zonal velocity GS	0.79	-0.38	-0.31	-0.33
NAD	0.81	-0.29	-0.39	-0.10
AC	0.58	0.88	0.53	0.82
meridional velocity GS	0.81	-0.41	-0.29	-0.36
NAD	0.79	-0.15	-0.07	-0.16
AC	0.54	0.80	0.22	0.80

TABLE 1. Correlation coefficient of the different modes with the observed fields (vorticity, zonal and meridional velocities and buoyancy) at ocean surface. SMOD stands for Surface mode, IMOD for sum of interior modes, BT for barotropic mode and BC1 for first baroclinic mode.

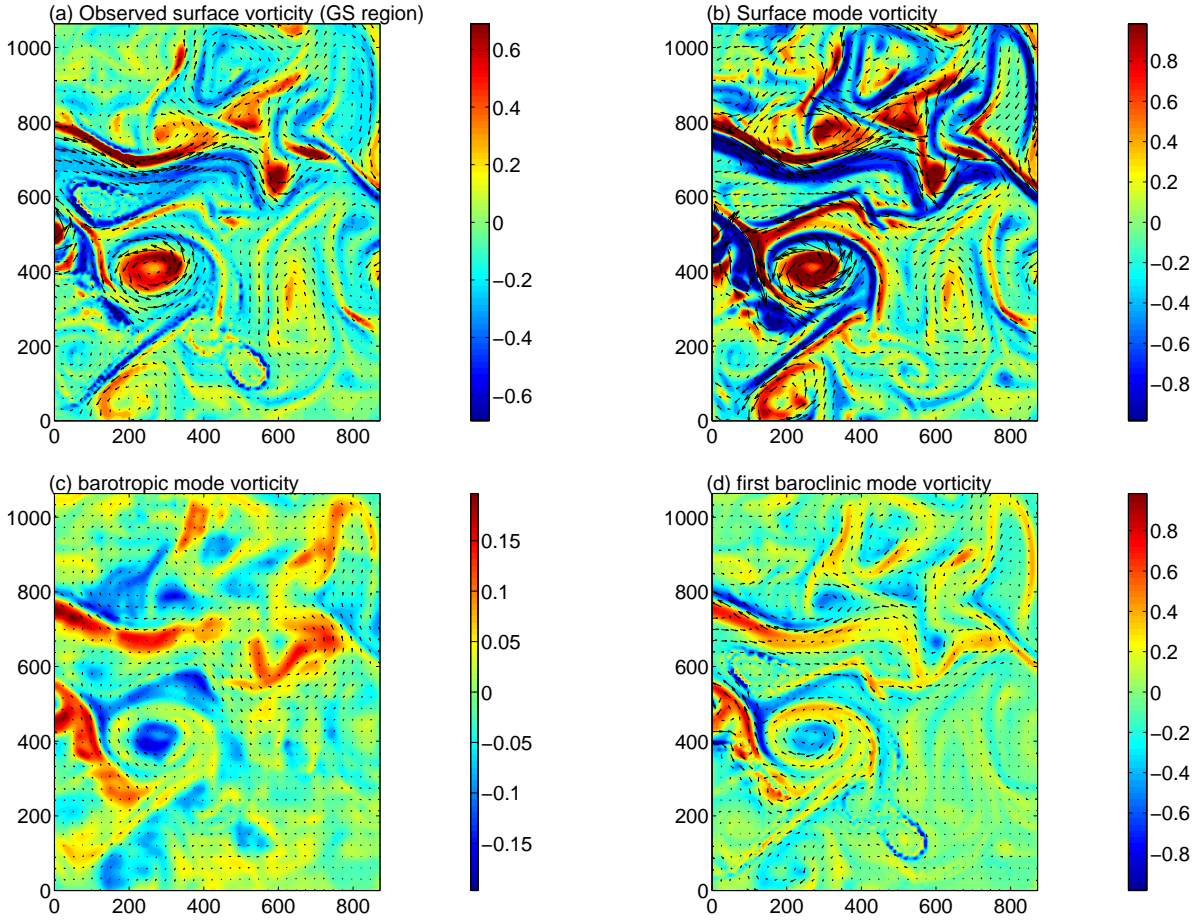


FIG. 6. (a) In color relative vorticity (divided by  $f_0$ ) at surface, arrows are horizontal velocities at the surface; (b) of the surface mode; (c) of the barotropic mode (complete method); (d) of first baroclinic mode (complete method). The same velocity scale was used to draw the arrows on each figure. The figure corresponds to the Gulf Stream region.

signal down to 600 m. The interior modes vanish at the surface but are quite important below 150 m, that is underneath the mixed layer base. The buoyancy variance is partitioned relatively evenly between the different baroclinic modes between 100 and 300 meters. Below, it is the first baroclinic mode that dominates.

To confirm the importance of the surface mode, the spatial fields at the surface can be examined. Figure 6 shows that the surface mode captures all the mesoscale signal in relative vorticity overestimating it, in particular at small scales. It has a strong correlation (0.80) with the true vorticity at the surface (Tab. 1). The first baroclinic mode is smaller and tends to diminish the high values of the surface mode (since it is of opposite sign in most regions and with a correlation of -0.42 with the true vorticity). The barotropic mode is negligible and captures larger scale structures. The velocity field displays similar characteristics although it down-weights the effect of small scales present in the vorticity field. This behavior can be interpreted as this: the surface mode is triggered by the surface buoyancy anomalies. Because of that, it will enhance small-scale structures through frontogenesis processes, and thus increases their vorticity signal.

The kinetic energy spectra of the different modes at the ocean surface are shown in Fig. 7a. The surface mode dom-

inates the surface KE signal in the range of 30 km (corresponding to  $k = 0.2 \text{ km}^{-1}$ ) to 800 km. Moreover it peaks at very large scales because of the presence of the large-scale buoyancy gradients. At small scales, it decays faster than the true kinetic energy. The KE spectrum due to interior modes is also larger than the observed surface KE spectrum for all wavelengths. The partition between vertical modes shows the dominance of the first baroclinic mode for scales smaller than 500 km. This mode is the dominant one for scales smaller than 30 km. For scales larger than 500 km, the barotropic mode is the most important. The barotropic signal cancels the surface mode contribution (remember that for these scales, the surface mode essentially gives a barotropic component).

The situation is much different at depth. At 460 m, both surface and interior modes have a positive correlation with the model vorticity field (Tab. 2). At this depth, the interior modes and the surface mode have comparable kinetic energies (Fig. 5a). The zonal and meridional velocity fields still correlate with the surface mode. However, the model velocity field does not correlate with the interior modes. This surprising result can be understood by looking at the KE spectra at 460 m (Fig. 7b). The surface mode dominates the interior modes only in a limited range of wavelengths (between

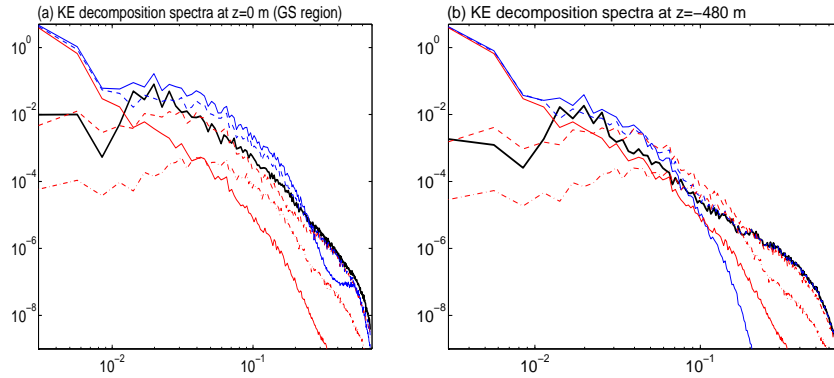


FIG. 7. Spectra of model kinetic energy (thick black line), surface mode KE (blue solid line), interior mode KE (blue dashed line) at  $z = 0$  m (a) and  $z = 460$  m (b). The red solid line is the barotropic mode, the red dashed line the first baroclinic and the red dash-dotted line the second baroclinic mode. For the regions GS.

Correlation	SMOD	IMOD	BT	BC1
vorticity GS	0.39	0.33	0.14	0.18
NAD	0.49	0.42	0.22	0.18
AC	0.24	0.94	0.41	0.83
zonal velocity GS	0.59	0.10	0.11	0.01
NAD	0.64	-0.04	-0.12	0.09
AC	0.53	0.91	0.71	0.87
meridional velocity GS	0.67	-0.06	-0.15	-0.06
NAD	0.59	0.22	0.25	0.05
AC	0.31	0.92	0.70	0.84

TABLE 2. Correlation between the different modes and vorticity, zonal and meridional velocity and buoyancy, at  $z = -480$  m. Same definition as in Fig. 1

100 km and 600 km) and then rapidly decays below 100 km. It will be positively correlated with the observed velocity field due to the energetic 100-600 scales. This is true for the vorticity field as well. Therefore, between 100 km and 600 km, the interior modes are anti-correlated with the surface mode in order to counteract the too strong value of the surface mode. For scales smaller than 100 km, the interior modes dominate the surface mode so that the interior modes will be positively correlated with the observed velocity field. It can be concluded that the interior modes have both positive and negative correlations with the true fields depending on the scales. The vorticity field highlights more small scales so that the positive correlation dominates. On the contrary, the velocity field weights equivalently the different scales and consequently both positive and negative correlations, so that the total correlation is close to zero, as observed (Tab. 2).

#### b. North Atlantic drift

The second active region is between  $40^\circ$ W and  $30^\circ$ W and  $40^\circ$ N and  $50^\circ$ N in the North Atlantic Drift. In this region, the kinetic energy is still intensified at the surface (not shown) and the buoyancy r.m.s. is intensified at 200 m underneath the mixed layer (Fig. 4a). The r.m.s. of the buoyancy is still better represented with the complete decomposition than with the incomplete decomposition and differences

can be observed down to 700 m. In the mixed layer, the complete decomposition gives correct r.m.s values, which was not the case for the Gulf Stream area. In the NAD region, the mixed layer is quite deep reaching 100 m depth. The r.m.s. of the difference between the different reconstructions and the observed buoyancy (Fig. 4b) confirms that the complete method better represents the buoyancy field, as expected.

As shown in Fig. 8, the situation at the ocean surface is rather similar to the Gulf Stream region. The velocity and vorticity fields of the surface mode are larger than the observed fields and small scales are strongly enhanced. The first baroclinic mode is in opposite phase to the surface mode, and the barotropic mode displays larger scale structures but of weaker intensity. This qualitative picture is confirmed by the correlations computed at ocean surface (Tab. 1) which are very similar to the correlations for the Gulf Stream region, except that the correlations of the first baroclinic mode with the surface flow are smaller. The reason is that the KE of the surface mode and the observed KE are closer in the NAD case than in the case of the GS region (compare the kinetic energy spectra of Fig. 9 with 7a). Henceforth the interior modes do not need to strongly anti-correlate with the surface mode, and thus with the observed fields. Apart from this difference, the surface kinetic spectra are very similar to the Gulf Stream region at the ocean surface (Fig. 9). At 460 m, the situation is qualitatively the same as in the GS region (not shown) and the spatial correlations present the same characteristics with weak correlations (smaller than 0.2) with the velocity fields (Tab. 2).

#### c. Azores current

The third region is an area between  $30^\circ$ W and  $20^\circ$ W and between  $30^\circ$ N and  $40^\circ$ N in the Azores current in the North East Atlantic. The kinetic energy is still intensified at the surface and decays with depth but with much smaller amplitude than the two other regions. Figure 4a shows that the buoyancy r.m.s. has also a much smaller amplitude. In this region, the complete and incomplete methods give almost the same buoyancy r.m.s for all depth except in the shallow mixed layer (50 m). Indeed, the r.m.s. of the difference between the observed buoyancy and its complete or incomplete

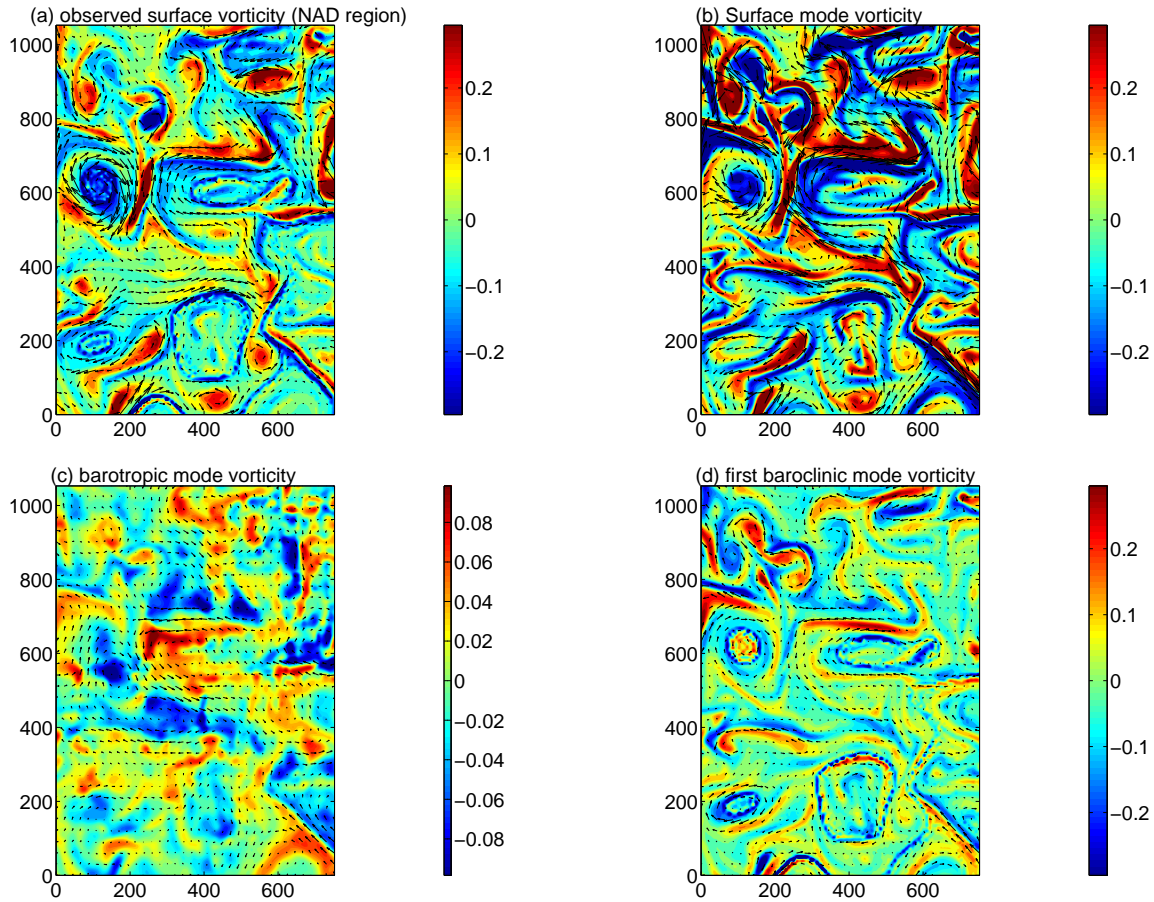


FIG. 8. Same meaning as for Fig. 6 but in region NAD.

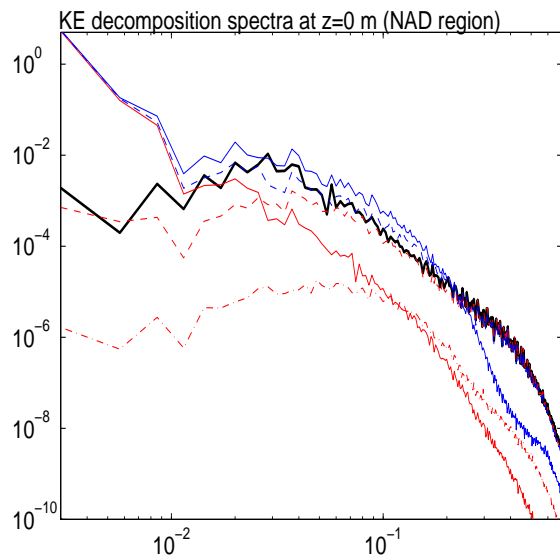


FIG. 9. Spectra of kinetic energy at the ocean surface for the NAD region. Same definition as in Fig. 7.

reconstruction shows a similar picture (Fig. 4b).

As might be expected, in this region, the decomposition gives a quite different result from the two other cases. The decomposition of the surface fields in Fig. 10 shows that the surface mode concentrates in small-scale frontal structures.

However it does not dominate at the ocean surface but has the same amplitude as the first baroclinic mode. The barotropic mode is still of weaker amplitude and at larger scales. Contrary to the other cases, the sum of interior modes correlates better with the observed vorticity and velocity fields at ocean surface than the surface mode (Tab. 1). In addition, the first baroclinic mode is strongly correlated with the surface fields for each dynamical variable.

The kinetic energy spectra (Fig. 11a) show that the interior modes dominate for almost all scales. Two exceptions are the larger scales where both surface and interior contributions have the same amplitude and scales close to 30 km for which the surface mode becomes as important as the interior modes. This confirms the visual inspection of Fig. 10. The interior contribution comes essentially from the first baroclinic mode and it has the same amplitude as the surface mode for all wavelengths (except for scales larger than 600 km). As a result, both the surface mode and the first baroclinic mode positively contribute to the observed surface flow, as confirmed by the correlation coefficients in Tab. 1. At depth, the interior modes have a quite strong correlation with the surface fields (around 0.9) whereas the surface mode has a weaker correlation (around 0.3) as shown in Tab. 2. The surface mode is quite weak for all wavelengths as can be seen in Fig. 11b and the first baroclinic mode dominates almost entirely the kinetic energy spectrum at this depth. The Azores region contrasts with the two other

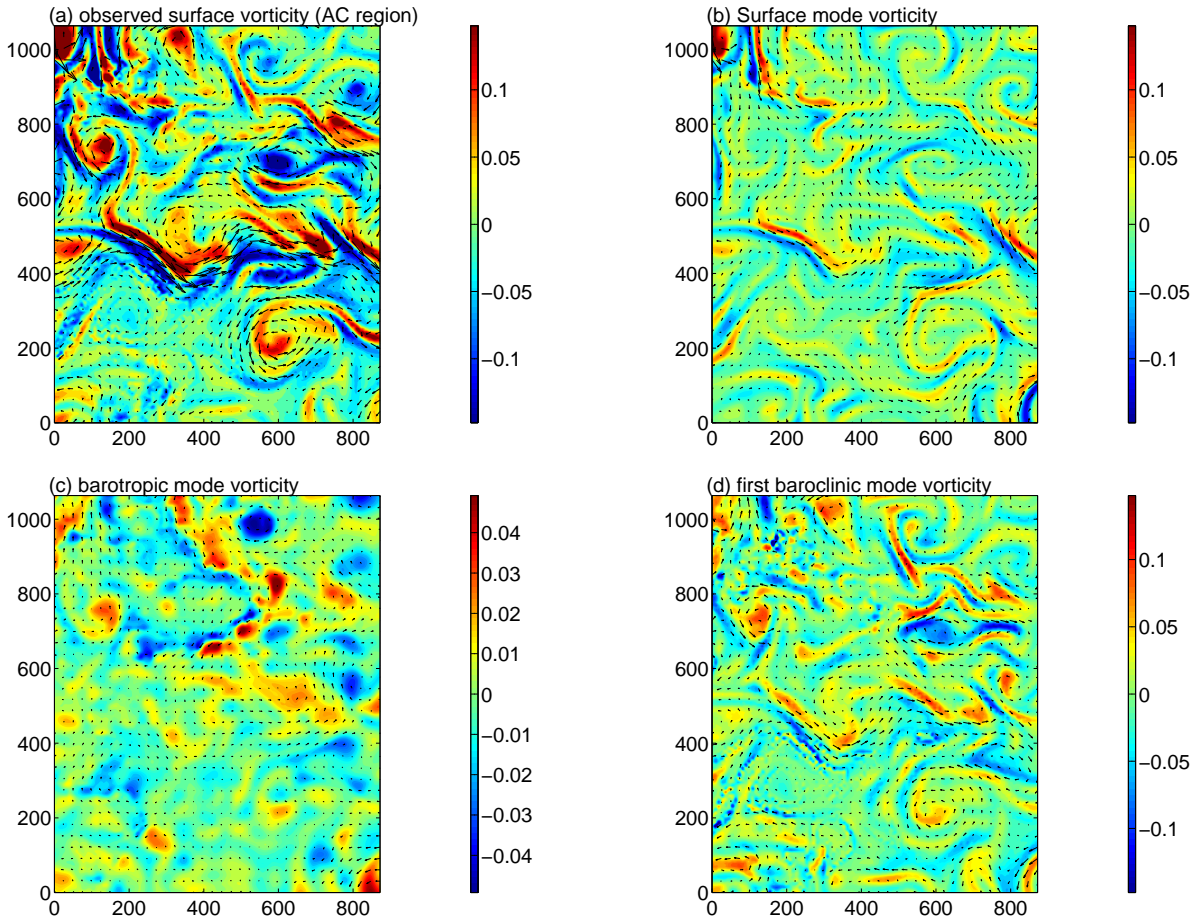


FIG. 10. Same meaning as for Fig. 6 but in region AC.

cases as, here, the energy is essentially captured by the first baroclinic mode and not by the surface mode. An examination of other regions shows this is not the sole case (see below).

## 5. Discussion

The three oceanic regions with strong mesoscale activity display some features in common and some marked differences: for all regions, the first baroclinic mode dominates over the other barotropic and baroclinic modes. This result is similar to conclusions of Wunsch (1997) and Smith and Vallis (2001) who respectively examined *in situ* data and simulations of QG turbulence. Also, in each region, kinetic energy is intensified at the ocean surface and buoyancy anomalies are intensified underneath the mixed layer. However, in two of the regions (Gulf Stream and North Atlantic Drift) the surface mode has a more intense signal than the interior modes while in the Azores current the first baroclinic mode is the larger one. This different behavior was found to be quite general for all regions studied in the North Atlantic. Indeed plotting the ratio of the r.m.s. of relative vorticity due to interior modes and to the surface mode (Fig. 12) shows that the surface mode dominates in a large fraction of the Atlantic ocean (19 regions of size  $6^\circ \times 5^\circ$  where the surface mode dominates against 12 regions where the interior

modes dominate). It is interesting to note that the surface mode dominates in the Gulf Stream and North Atlantic current, while the interior modes dominate in the recirculating branch of the gyre (Azores current and Portugal current).

Theoretical developments of Lapeyre and Klein (2006a) who investigated the link between surface and interior dynamics may provide some interpretation of this result and may explain the localization of regions dominated by the first baroclinic mode or by the surface mode. As explained in Section 2, the PV inversion problem can be decomposed into two sub-problems (9) and (10). Using the assumption that large-scale PV and surface buoyancy meridional gradients are the first source of mesoscale anomalies of PV and surface buoyancy, one obtains

$$\left( \frac{\partial}{\partial t} + \mathbf{u} \cdot \nabla \right) PV' = -v \frac{\partial \overline{PV}}{\partial y} \quad (27a)$$

$$\left( \frac{\partial}{\partial t} + \mathbf{u}_s \cdot \nabla \right) b'_s = -v_s \frac{\partial \overline{b}_s}{\partial y} \quad (27b)$$

where  $PV'$  and  $b'_s$  are mesoscale anomalies and  $\overline{PV}$  and  $\overline{b}_s$  are large-scale variables. Considering that the velocity field has slow variations in the vertical (at least in the upper oceanic layers), Lapeyre and Klein (2006a) derived a rela-

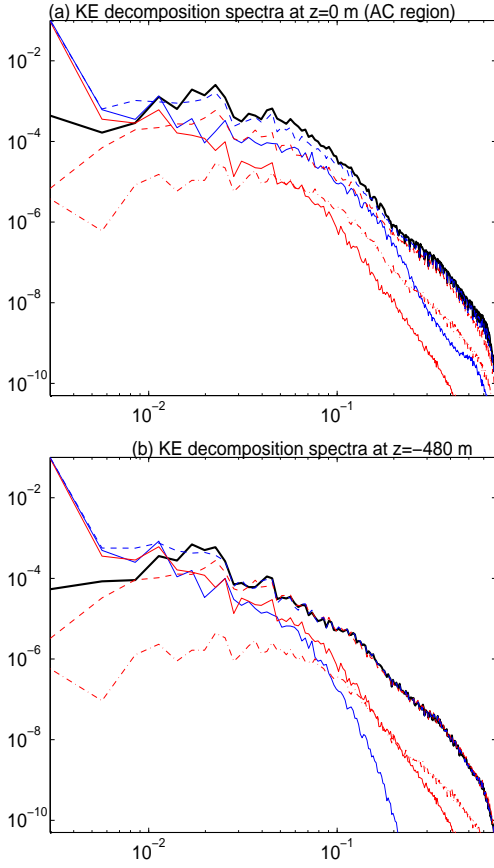


FIG. 11. Spectra of kinetic energy at the ocean surface (a) and at 460 m (b) for the AC region. Same definition as in Fig. 7.

tion between the anomalies

$$PV' \approx \frac{\partial_y \overline{PV}}{\partial_y \overline{b_s}} b'_s \quad (28)$$

The reason is that the velocity field advects and stirs the PV and surface buoyancy down their mean gradient in the same manner. The large-scale PV gradient is proportional in first approximation to the buoyancy gradient  $\partial_y \overline{PV} \approx \partial_z (f_0^2 N^{-2} \partial_z (\partial_y \overline{b}))$  so that there exists a strong correlation between  $\partial_y \overline{PV}$  and  $\partial_y \overline{b_s}$ . The stirring process then drives the correlation that exists at large-scale to small scales through the tracer cascades of interior PV and surface buoyancy. The inversion of PV that gives  $\psi_{int}$  will thus be correlated to the inversion of surface buoyancy that gives  $\psi_{sur}$ .

To confirm this result, the regression of  $PV'$  on  $b'_s$  can be compared with the regression of  $\partial_y \overline{PV}$  on  $\partial_y \overline{b_s}$  (that is noted  $\Gamma$  for future use) choosing 400 km as the wavelength of separation between meso and large scales (fields have been respectively high and low pass filtered). Here, values underneath the mixed layer (ML) were chosen for surface buoyancy values in order to reflect proper QG dynamics since surface buoyancy reflects either surface forcing or buoyancy underneath the ML depending on the wind conditions (Klein and Hua 1990). This has for effect to increase the correlation between  $PV'$  and  $b'_s$  as expected. As shown in Fig. 13a, in the three oceanic regions, the two regressions qualitatively match each other for the first 1000 meters. Re-

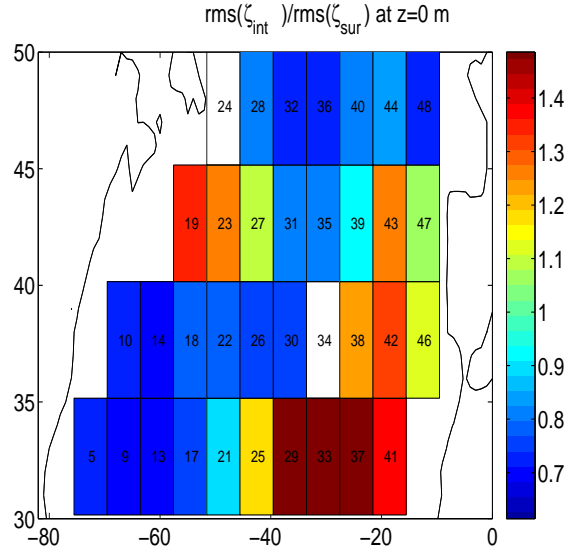


FIG. 12. Ratio of rms of relative vorticity due to interior modes and rms of surface-mode relative vorticity taken at surface. The numbers inside each box correspond to their identification number.

lation (28) is further confirmed by the quite strong positive or negative correlations between interior PV anomalies and surface buoyancy anomalies (Fig. 13b). It can also be noted that the sign of the correlation is the same as the regression of  $\partial_y \overline{PV}$  on  $\partial_y \overline{b_s}$  (compare Fig. 13a and b).

As a result, it can be expected that the sign and amplitude of  $\Gamma$ , the regression of  $\partial_y \overline{PV}$  on  $\partial_y \overline{b_s}$ , should impact the relation between  $\psi_{int}$  and  $\psi_{sur}$ . Figure 14a shows the scatterplot of  $\Gamma$  and the ratio of r.m.s of vorticities due to  $\psi_{int}$  and  $\psi_{sur}$  evaluated at the ocean surface. For small values of  $\Gamma$ , there is a tendency towards dominance of vorticity of the surface mode, while for large values the interior modes tend to dominate. However there is a strong asymmetry between positive and negative values of  $\Gamma$ . Regions dominated by interior modes correspond to negative  $\Gamma$ . In these regions, the correlation between  $-\Gamma$  and surface and interior mode vorticity ratio is 0.75 which indicates that the large scale gradients are important in determining the relative importance of each mode as expected. On the other hand, regions dominated by the surface mode correspond mainly to positive  $\Gamma$ . For these regions, the correlation between the interior/surface mode ratio and  $\Gamma$  is only 0.6 (removing box 21, 28 and 44 from the computation of the correlation coefficient).

Since, for negative  $\Gamma$ , the interior modes should dominate the surface signal, the vorticity due to the interior modes should be positively correlated with the observed vorticity at ocean surface. On the contrary, for positive  $\Gamma$ , the surface mode will dominate. Since the surface buoyancy behaves as a negative PV source  $-(f_0/N^2)b_s\delta(z)$  (see Bretherton 1966; Lapeyre and Klein 2006a) and since in these regions  $PV'$  and  $b'_s$  are positively correlated (due to  $\Gamma > 0$ ),  $\psi_{int}$  and  $\psi_{sur}$  will be anti-correlated. Therefore, the vorticity due to the interior modes can be expected to be negatively correlated with the observed vorticity. Fig. 14b confirms this reasoning as it shows that  $\Gamma$  and the correlation of the inte-

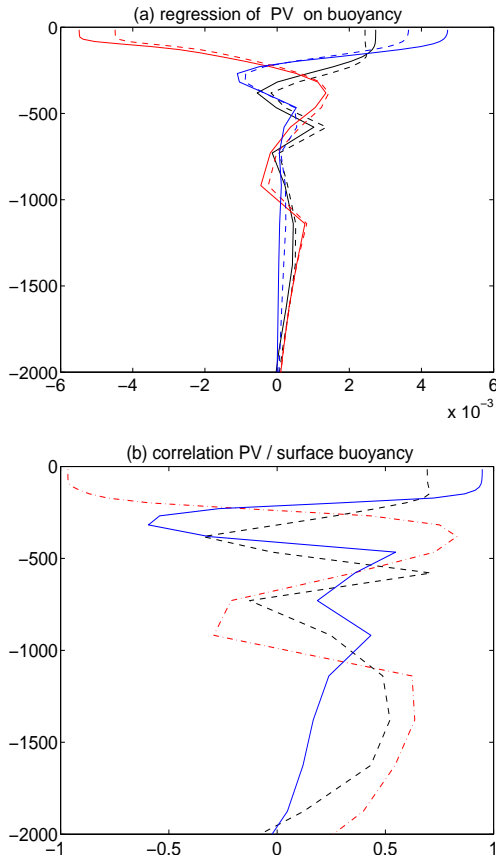


FIG. 13. (a) Regression of  $PV'(x, y, z)$  on  $b'_s(x, y)$  (solid line) and the regression of  $\partial_y \overline{PV}(x, y, z)$  on  $\partial_y \overline{b}_s(x, y)$  (dashed line) as a function of depth  $z$ . (b) Spatial correlation coefficient of  $PV'(x, y, z)$  with  $b'_s(x, y)$  as a function of depth  $z$ . For each panel, blue curves correspond to Gulf Stream region, red curves to the Azores region and black curve to the North Atlantic Drift.

rior mode vorticity and the observed vorticity taken at  $z = 0$  vary in opposite directions. At 460 m, the interior modes begin to dominate the surface trapped mode and the correlation is positive through the Atlantic (not shown). The surface mode has therefore a weak influence at depth.

We thus see that the dominance of the surface mode or the first baroclinic mode depends on the large-scale forcings. As a result, the velocity and vorticity fields observed at the ocean surface do not in general reflect the first baroclinic mode. This is not an artifact of the decomposition method because the method takes into account the thermal wind balance and is consistent with QG dynamics, while an incomplete decomposition would not fulfill the requirement of non-vanishing surface buoyancy. The incomplete decomposition would project the surface mode signal onto the first baroclinic mode. This would tend to overestimate the role of the first baroclinic mode in the dynamics. Indeed, the first baroclinic mode dominates when doing an incomplete decomposition for the GS and NAD regions (not shown).

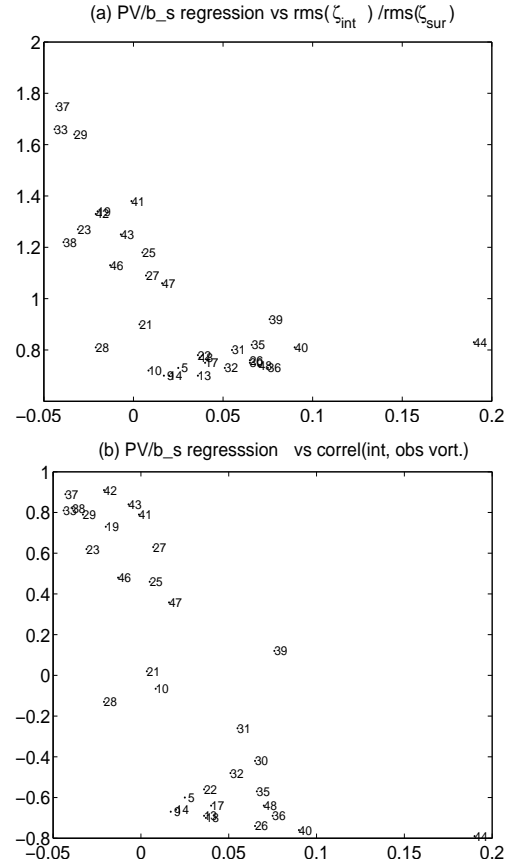


FIG. 14. (a) Scatter plot of  $\Gamma$  (abscissa) (in  $\text{km}^{-1}$ ) and ratio of r.m.s. of  $\zeta_{int}$  and r.m.s. of  $\zeta_{sur}$ . On both figure, each point corresponds to one region of Fig. 12 identified by its number. (b) Scatter plot of  $\Gamma$  (abscissa) (in  $\text{km}^{-1}$ ) and correlation coefficient of observed vorticity at surface and interior mode vorticity (ordinate).

## 6. Conclusion

In this paper, it has been shown that the decomposition of a quasigeostrophic flow into barotropic and baroclinic modes is not complete because it does not satisfy the non-vanishing buoyancy at the ocean surface. To take into account this component, a mode with zero quasi-geostrophic potential vorticity needs to be added, that fulfils the boundary condition at the ocean surface. This mode is surface trapped (or surface intensified) and corresponds to the SQG dynamics (Held et al. 1995). It is not orthogonal to the baroclinic mode and projects essentially on the first baroclinic mode at mesoscales and on the barotropic mode at larger scales.

A complete decomposition (interior barotropic, baroclinic modes and surface-trapped mode) has been performed for a numerical simulation of the Atlantic Ocean that resolves mesoscale dynamics. The surface mode contribution was found to be as large as the contribution of the first baroclinic mode for all the Atlantic ocean for the upper oceanic layers. The contributions of the barotropic or the other baroclinic modes are systematically weaker. In the most energetic part of the North Atlantic (Gulf Stream and North Atlantic Drift areas), the surface flow mostly reflects the surface mode. Since the surface buoyancy plays the role of a Dirac func-

tion in PV and since the mesoscale flow is primarily forced by baroclinic instability, it can be shown that the large-scale gradients of PV and surface buoyancy determine which (first baroclinic or surface) is the dominant mode.

Therefore satellite altimetry does not always reflect the first baroclinic mode as claimed by different authors (Stammer 1997; Scott and Arbic 2007). This strengthens in part the applicability of the effective SQG method (Lapeyre and Klein 2006a; LaCasce and Mahadevan 2006; Isern-Fontanet et al. 2006, 2007) which is a method based on the surface mode to reconstruct the dynamics of the upper ocean from surface buoyancy only using a constant  $N^2$ . Finally these results exacerbate the need to understand the coupling between interior PV anomalies and surface buoyancy anomalies, and in particular the observed anticorrelation between the first baroclinic mode and the surface mode.

*Acknowledgments.* The author wants to acknowledge stimulating discussion about the surface dynamics with Patrice Klein, Shafer Smith and Rob Scott. Also Matthew Hecht and Patrice Klein have provided the numerical simulation used in this paper.

### Appendix. Technical aspect of the decomposition

The streamfunction and buoyancy fields need to be properly balanced to solve at the same time (9) and (10). In general, this is not strictly true (in particular in the mixed layer). To impose thermal wind balance, the method proposed by Rudnick (1996) was followed, which consists in writing

$$\psi = \phi + R \quad (29)$$

with

$$R = \frac{1}{f_0} \int_{-H}^z b \, dz \quad (30)$$

$H$  is chosen to be  $H = 3600$  m. If the functional

$$\int_{-H}^z \iint ((-\partial_y \psi - u_{obs})^2 + (\partial_x \psi - v_{obs})^2) \, dx dy dz \quad (31)$$

is minimized, a constraint for  $\phi$  is obtained,

$$\nabla^2 \phi = \frac{1}{H} \int_{-H}^0 (\zeta_{obs} - \nabla^2 R) dz \quad (32)$$

The streamfunction  $\phi + R$  is in thermal wind balance with the buoyancy  $b$  and this gives a better result for the reconstruction. It has been checked that the streamfunction  $\phi + R$  is very similar to the real one (not shown).

The decomposition (16) with (17) problem can be discretized and solved through matrix diagonalization and using the fact that  $\partial_z \hat{E}(z=0) = 1$  is mathematically equivalent to a Dirac function in the right hand side of (17) (see Bretherton 1966; Lapeyre and Klein 2006a). If  $\hat{E}(k, z)$  is projected on each interior mode  $F_j$ , one obtains  $n + 1$  equations with  $n + 2$  unknowns ( $\hat{\alpha}_j(\mathbf{k})$  and  $\hat{\gamma}(\mathbf{k})$ ),

$$\hat{\alpha}_j(\mathbf{k}) + \hat{\gamma}(\mathbf{k}) \int_{-H}^0 F_j(z) \hat{E}(k, z) dz = \int_{-H}^0 F_j(z) \hat{\psi}(\mathbf{k}, z) dz \quad (33)$$

for  $j = 0$  to  $n$ . The last equation is found by minimizing the functional

$$I = \iint_{z_0}^0 \left| \hat{b}(\mathbf{k}, z) - f_0 \sum_{j=0}^n \hat{\alpha}_j(\mathbf{k}) \frac{\partial F_j}{\partial z}(z) - \hat{\gamma}(\mathbf{k}) f_0 \frac{\partial \hat{E}}{\partial z}(k, z) \right|^2 dz dk \quad (34)$$

Using (33), one obtains

$$I = \iint_{z_0}^0 \left| \hat{b}(\mathbf{k}, z) - f_0 \sum_{j=0}^n \hat{\psi}_j(\mathbf{k}) \frac{\partial F_j}{\partial z}(z) - \hat{\gamma}(\mathbf{k}) f_0 \left( \frac{\partial \hat{E}}{\partial z}(k, z) - \sum_{j=0}^n \hat{E}_j(\mathbf{k}) \frac{\partial F_j}{\partial z}(z) \right) \right|^2 dz dk \quad (35)$$

where

$$\hat{\psi}_j(\mathbf{k}) = \int_{-H}^0 F_j(z) \hat{\psi}(\mathbf{k}, z) dz \quad (36a)$$

$$\hat{E}_j(k) = \int_{-H}^0 F_j(z) \hat{E}(k, z) dz \quad (36b)$$

The minimum of the functional is reached when  $DI/D\hat{\gamma}(\mathbf{k}) = 0$ , i.e.

$$\hat{\gamma}(\mathbf{k}) \int_{z_0}^0 \left| \frac{\partial \hat{E}}{\partial z}(k, z) - \sum_{j=0}^n \hat{E}_j(k) \frac{\partial F_j}{\partial z}(z) \right|^2 dz = \int_{z_0}^0 \left( \frac{\hat{b}(\mathbf{k}, z)}{f_0} - \sum_{j=0}^n \hat{\psi}_j(\mathbf{k}) \frac{\partial F_j}{\partial z}(z) \right) \times \left( \frac{\partial \hat{E}}{\partial z}(z) - \sum_{j=0}^n \hat{E}_j(k) \frac{\partial F_j}{\partial z}(z) \right) dz \quad (37)$$

which determines  $\hat{\gamma}(\mathbf{k})$ . As the surface mode is trapped in the upper oceanic layers, the integrals are evaluated between the surface and  $z_0 = -400$  m. This method is more robust than a method that would instead use an equation for the buoyancy at a particular level. In this case, the solution is strongly sensitive to the choice of the vertical level (not shown).

The computation of only 8 vertical modes ( $n = 7$ ) has been considered because the higher modes are not numerically well resolved (due to the vertical discretization on 32 levels between the surface and 3600 m in the POP simulation). Also, the vertical profiles of the mean  $N^2$  have been smoothed following Emery et al. (1984):  $N^2$  is interpolated on a grid 2.4 times thinner, smoothed with a Gaussian weight over 5 grid points and then reinterpolated on the original grid. Values of  $N^2$  smaller than  $10^{-7} \text{ s}^{-2}$  are replaced by  $10^{-7} \text{ s}^{-2}$ . Finally  $\hat{E}$  is computed on a grid 4 times thinner so that the Dirac function of PV can be replaced by a step function. Then it is interpolated back on the original grid.

## REFERENCES

- Brachet S., P. Y. Le Traon, and C. Le Provost, 2004: Mesoscale variability from a high resolution model and from altimeter data in the north atlantic ocean. *J. Geophys. Res.*, **109**, C12025, doi:10.1029/2004JC002360.
- Bretherton F. P., 1966: Critical layer instability in baroclinic flows. *Q. J. R. Meteorol. Soc.*, **92**, 325–334.
- Bryan F. O., M. W. Hecht, and R. D. Smith, 2007: Resolution convergence and sensitivity studies with North Atlantic circulation models. Part I: The western boundary current system. *Ocean Modelling*, **16**, 141–159.
- Capet X., P. Klein, B. L. Hua, G. Lapeyre, and J. C. McWilliams, 2007: Surface kinetic and potential energy transfer in SQG dynamics. *J. Fluid Mech.*, in revision.
- Charney J., 1971: Geostrophic turbulence. *J. Atmos. Sci.*, **28**, 1087–1095.
- Chelton D. B., R. A. De Szoeke, M. G. Schlax, K. El Naggar, and N. Siwertz, 1998: Geographical variability of the first baroclinic Rossby radius of deformation. *J. Phys. Oceanogr.*, **28**, 433–460.
- De Mey P. and A. R. Robinson, 1987: Assimilation of altimeter eddy fields in a limited-area quasi-geostrophic model. *J. Phys. Oceanogr.*, **17**, 2280–2293.
- Dutton J. A., 1974: The nonlinear quasi-geostrophic equation: existence and uniqueness of solutions on a bounded domain. *J. Atmos. Sci.*, **31**, 422–433.
- Emery W. J., W. G. Lee, and L. Magaard, 1984: Geographic and seasonal distributions of Brunt-Väisälä frequency and Rossby radii in the North Pacific and the North Atlantic. *J. Phys. Oceanogr.*, **14**, 294–317.
- Flierl G. R., 1978: Models of vertical structure and the calibration of two-layer models. *Dyn. Atmos. Oceans*, **2**, 341–381.
- Gill A.: 1984, *Dynamics of Atmospheres and Oceans*. Academic Press.
- Held I. M., R. L. Panetta, and R. T. Pierrehumbert, 1985: Stationary external Rossby waves in vertical shear. *J. Atmos. Sci.*, **42**, 865–883.
- Held I. M., R. T. Pierrehumbert, S. T. Garner, and K. L. Swanson, 1995: Surface quasi-geostrophic dynamics. *J. Fluid Mech.*, **282**, 1–20.
- Hua B. L. and D. B. Haidvogel, 1986: Numerical simulations of the vertical structure of quasi-geostrophic turbulence. *J. Atmos. Sci.*, **43**, 2923–2936.
- Isern-Fontanet J., B. Chapron, G. Lapeyre, and P. Klein, 2006: Potential use of microwave sea surface temperatures for the estimation of ocean currents. *Geophys. Res. Lett.*, **33**, L24608, doi:10.1029/2006GL027801.
- Isern-Fontanet J., G. Lapeyre, P. Klein, B. Chapron, and M. W. Hecht, 2007: 3D reconstruction of oceanic mesoscale currents from surface information. Submitted to *J. Geophys. Res.*
- Klein P. and B. L. Hua, 1990: The mesoscale variability of the sea surface temperature: an analytical and numerical model. *J. Mar. Res.*, **48**, 729–763.
- Klein P., B. L. Hua, G. Lapeyre, X. Capet, S. L. Gentil, and H. Sasaki, 2007: Upper ocean turbulence from high 3-d resolution simulations. *J. Phys. Oceanogr.*, in revision.
- LaCasce J. H. and A. Mahadevan, 2006: Estimating sub-surface horizontal and vertical velocities from sea surface temperature. *J. Mar. Res.*, **64**, 695–721.
- Lapeyre G. and P. Klein, 2006a: Dynamics of the upper oceanic layers in terms of surface quasigeostrophy theory. *J. Phys. Oceanogr.*, **36**, 165–176.
- 2006b: Impact of the small-scale elongated filaments on the oceanic vertical pump. *J. Mar. Res.*, **64**, 935–951.
- Lapeyre G., P. Klein, and B. L. Hua, 2006: Oceanic restratification forced by surface frontogenesis. *J. Phys. Oceanogr.*, **36**, 1577–1590.
- McWilliams J. C. and J. H. S. Chow, 1981: Equilibrium geostrophic turbulence I: a reference solution in a  $\beta$ -plane channel. *J. Phys. Oceanogr.*, **11**, 921–949.
- McWilliams J. C., W. B. Owens, and B. L. Hua, 1986: An objective analysis of POLYMODE local dynamics experiment. Part I: general formalism and statistical model selection. *J. Phys. Oceanogr.*, **16**, 483–504.
- McWilliams J. C. and C. Y. Shen, 1980: Mesoscale modal coupling. *J. Phys. Oceanogr.*, **10**, 741–752.
- Philander S. G. H., 1978: Forced oceanic waves. *Rev. Geophys.*, **16**, 15–46.
- Rudnick D. L., 1996: Intensive surveys of the azores front. 2. Inferring the geostrophic and vertical velocity fields. *J. Geophys. Res.*, **101**, 16,291–16,303.
- Schlosser F. and C. Eden, 2007: Diagnosing the energy cascade in a model of the North Atlantic. *Geophys. Res. Lett.*, **34**, L02604, doi: 10.1029/2006GL027813.
- Scott R. B. and B. K. Arbic, 2007: Spectral energy fluxes in geostrophic turbulence: Implications for ocean energetics. *J. Phys. Oceanogr.*, **37**, 673–688.
- Scott R. B. and F. Wang, 2005: Direct evidence of an oceanic inverse kinetic energy cascade from satellite altimetry. *J. Phys. Oceanogr.*, **35**, 1650–1666.
- Smith K. S. and G. K. Vallis, 2001: The scales and equilibration of midocean eddies: freely evolving flow. *J. Phys. Oceanogr.*, **31**, 554–571.
- Smith R., M. Maltrud, F. Bryan, and M. Hecht, 2000: Numerical simulation of the North Atlantic Ocean at  $1/10^\circ$ . *J. Phys. Oceanogr.*, **30**, 1532–1561.
- Stammer D., 1997: Global characteristics of ocean variability estimated from regional TOPEX/POSEIDON altimeter measurements. *J. Phys. Oceanogr.*, **27**, 1743–1769.
- Tung K. K. and W. T. Welch, 2001: Remarks on Charney's note on geostrophic turbulence. *J. Atmos. Sci.*, **58**, 2009–2012.
- Wunsch C., 1997: The vertical partition of oceanic horizontal kinetic energy. *J. Phys. Oceanogr.*, **27**, 1770–1794.